Received: 30 October 2018 | Revised: 27 June 2019 | Accepted: 9 August 2019

DOI: 10.1002/pip.3190

RESEARCH ARTICLE

WILEY PROGRESS IN PHOTOVOLTAICS

Tunnel oxide passivating electron contacts for high-efficiency n-type silicon solar cells with amorphous silicon passivating hole contacts

HyunJung Park[1] | Youngseok Lee[2] | Se Jin Park[1] | Soohyun Bae[1] | Sangho Kim[2] | Donghyun Oh[3] | Jinjoo Park[3] | Youngkuk Kim[3] | Hwanuk Guim[4] | Yoonmook Kang[5] | Hae-Seok Lee[5] | Donghwan Kim[1,5] | Junsin Yi[3]

[1] Department of Materials Science and Engineering, Korea University, Seoul 02841, Republic of Korea

[2] Department of Energy Science, Sungkyunkwan University, Suwon 16419, Republic of Korea

[3] College of Information and Communication Engineering, Sungkyunkwan University, Suwon 16419, Republic of Korea

[4] Center for Electron Microscopy Research, Korea Basic Science Institute, Daejeon 305-333, Republic of Korea

[5] KU-KIST Green School, Graduate School of Energy and Environment, Korea University, Seoul 02841, Republic of Korea

Correspondence
Donghwan Kim, Department of Materials Science and Engineering, Korea University, Seoul 02841, Republic of Korea.
Email: donghwan@korea.ac.kr

Junsin Yi, College of Information and Communication Engineering, Sungkyunkwan University, Suwon 16419, Republic of Korea.
Email: junsin@skku.edu

Funding information
National Research Foundation, Grant/Award Number: NRF-2017M1A2A2087351; Korea Institute of Energy Technology Evaluation and Planning, Grant/Award Numbers: 20154030200760 and 20163030014020

Abstract

This study proposes a hybrid solar cell structure for a highly efficient silicon solar cell obtained by combining two passivating contact structures, namely, a heterojunction and polysilicon passivating contact. Given that the major cause of the loss in efficiency of crystalline silicon solar cells is carrier recombination at the metal-semiconductor junction, a passivating contact having high-quality passivation and a low contact resistance was introduced. In this study, two major passivating contact solar cells were combined. By applying an intrinsic thin amorphous silicon layer at the front and a tunneling oxide at the rear, a hybrid silicon solar cell with an efficiency of 21.8% was fabricated. Moreover, to evaluate the potential efficiency limit and to suggest methods for improving the cell performance of the proposed amorphous silicon emitter tunnel oxide back contact structure, the cell efficiency was simulated, and the result indicated that an efficiency of 26% could be achieved by controlling the thickness and resistivity of the wafer.

KEYWORDS

heterojunction, high efficiency, hybrid, passivating contact, silicon solar cell

1 | INTRODUCTION

A solar cell comprises a light-absorbing semiconductor and two selective contacts that extract holes on one side and electrons on the other side. A major cause of the loss in the efficiency of solar cells is the carrier recombination induced by defects at the metal-semiconductor interface. To reduce the recombination losses and increase the efficiency, a passivation layer can be inserted between the metal and the semiconductor. The passivating structure between the metal and the semiconductor is referred to as the passivating (or passivated) contact, and it provides high-quality passivation above an open-circuit voltage (V_{OC}) of 700 mV, in addition to a low contact resistivity over the full area.[1-8] The required conditions for passivating contacts are as follows: (a) the contact resistivity ($\rho_{contact}$) should be low, and (b) the

HyunJung Park and Youngseok Lee contributed equally.

recombination current density of the contacts ($J_{O,\ contact}$) should be prevented by the high-quality passivation of the interface. Given that other recombination pathways are reduced, these two contact parameters have a significant influence on the efficiency of solar cells.

The most commonly known example of a solar cell with a passivating contact is the heterojunction solar cell with an intrinsic thin film (HIT), which achieved an impressive V_{OC} of 750 mV and maximum efficiency of 26.7% with an interdigitated back contact (IBC) structure[9,10] and 24.7% with both contact structures.[11] The high V_{OC} was attributed to the excellent surface passivation of the thin intrinsic amorphous silicon layer. However, the heterojunction solar cell requires a low-temperature process below 250°C and therefore necessitates dedicated low-temperature processes such as transparent conductive oxide deposition and metallization using a low-temperature firing paste.[12-16] Management of the overall process temperature is necessary to obtain outstanding HIT solar cells performance.

Compared with a silicon heterojunction (SHJ) solar cell, a passivating contact composed of a doped polysilicon layer and thin silicon oxide is a promising method for the realization of high-efficiency passivating contact solar cells. The poly-Si/SiO_x passivating contact is categorized according to the method used to form the polysilicon layer: (a) a crystallized amorphous silicon layer referred to as a tunnel oxide passivated contact (TOPCon),[5,17] (b) an in situ poly-crystallized silicon layer referred to as semi-insulating polycrystalline silicon (SIPOS),[18,19] or polysilicon on oxide (POLO).[6,20-23] Recently, Fraunhofer ISE reported a TOPCon cell with an efficiency of 25.7%,[24] which was based on the combination of a boron-diffused front structure and a tunnel oxide passivating contact at the rear, which is the highest efficiency of c-Si solar cells contacted on both sides. The highest efficiency using a poly-Si/SiO_x passivating contact is 26.1% with a back contact POLO structure, which was reported by Institute for Solar Energy Research (ISFH, Hamelin, Germany).[23]

However, the TOPCon and POLO processes include photolithography, liftoff, and evaporation, which makes commercialization difficult because of increased production cost and complex fabrication process. Moreover, the front emitter diffusion process using BBr_3 diffusion or boron implantation should be suitably controlled, which is also difficult. For the realization of highly efficient n-type silicon solar cells, the front boron emitter presents several challenges. First, metallization for achieving low contact resistivity for the boron emitter is difficult because the conventional Ag paste cannot be used, and Ag-Al paste induces high recombination current density for the boron emitter contact.[25-28] Fraunhofer ISE also used the Ti/Pd/Ag evaporation method employing photolithography for the front contact.[29] Second, it is difficult to control the boron doping profile for low recombination current density, and a number of research studies have shown that this is a barrier for the industrialization of n-type silicon solar cells.[30,31] In addition, although IBC solar cells have reached a record efficiency of over 26%, the process flow is complicated and uses ion implantation and the photolithography method to realize the pattern at the rear side, which is challenging for commercialization.[23,32] Using both contact structures for achieving high efficiency offers the advantages of low fabrication cost and fewer process steps compared with IBC cells. To increase the possibility of the commercialization of the passivating contact, a hybrid solar cell that combines both POLO and SHJ solar cells is proposed, which allows for the realization of a low-cost, high-efficiency structure. This structure is referred to as the amorphous silicon emitter and tunnel oxide back contact hybrid cell. The first hybrid cell fabricated using a combination of SHJ and poly-Si passivated contact was published by Limodio et al. However, their procedure was different from ours in the following ways: (a) Limodio et al used float zone (FZ) silicon wafer and complicated fabrication steps including ion implantation and photolithography, which still means that this method would have limited commercial application. (b) The hybrid cell of Limodio et al consists of a rear emitter with SiO_x/*p* + poly-Si and front back-surface field (BSF) with *i*-*a*-Si/*n* + *a*-Si:H[33] while our hybrid cell consists of a front emitter with *i*-*a*-Si:H/*p* + *a*-Si:H and a rear BSF with SiO_x/*n* + poly-Si contact. Thus, we suggest a new hybrid cell structure that is more commercially viable with a fabrication method that has one step less and without using the boron implantation method.

The motivations of our research regarding the hybrid cell are (a) to suggest the possibility of a new hybrid silicon solar cell structure, with simulation results showing the efficiency that can be achieved using the hybrid cell, (b) to suggest a new structure that can be used in the industry, and (c) to utilize the gettering effect by employing a hybrid cell structure that combines the high- and low-temperature processes,[7] which is the advantage of using our hybrid cell structure compared with the SHJ cell.

Further, our research on the hybrid cell aims (a) to show a method for improving the cell efficiency in the hybrid structure, (b) at a realization of greater than 21% efficiency using the hybrid cell structure, (c) to conduct detailed studies on both high-quality passivating contacts, that is, heterojunctions and poly-Si/SiO_x contacts, which are in the mainstream of recent photovoltaic (PV) research, (d) to describe the fabrication method for the hybrid cell with a detailed experimental procedure, and (e) to suggest the way to improve the efficiency of the hybrid cell.

In this study, a hybrid cell with a poly-Si passivating contact on the rear side and a heterojunction structure on the front side was realized using a hydrogenated amorphous silicon (*a*-Si:H) emitter. For the rear structure, the passivation quality of the poly-Si contact was improved using two different doping methods, to obtain *n* + poly-Si: $POCl_3$-diffused poly-Si and in situ P-doped poly-Si. To investigate the cause of the improved passivation, the grain size and doping profile of the poly-Si passivating contact were analyzed. At the front side, two types of emitter layers were used, namely, p-type *a*-Si:H and p-type microcrystalline silicon oxide (*μc*-SiO:H). It is common knowledge that the main limitation to the efficiency of the SHJ cell type is due to parasitic absorption in the *a*-Si:H layer and transparent conducting oxide layer.[34,35] Hydrogenated microcrystalline silicon oxide (*μc*-SiO:H) has been applied as an emitter material in SHJ solar cells due to its lower optical absorption coefficients and better electrical properties when compared with *a*-Si:H.[36-38] Moreover, *μc*-SiO:H was employed to reduce the parasitic absorption in the doped *a*-Si layer of the hybrid cells. The hybrid cells were then fabricated, and their performance was evaluated.

2 | EXPERIMENTAL DETAILS

In this study, hybrid solar cells with a designated area of 10.24 cm^2 (3.2 cm × 3.2 cm) were fabricated on commercially available (100)-oriented n-type Cz wafers with thicknesses of 200 μm, and resistivities ranging from 1 to 2 Ω·cm. Given that the front side, which contains amorphous silicon, limits the process temperature; the manufacturing process of the hybrid cell proceeds from the rear side process, which involves high-temperature annealing. A schematic of the hybrid cell structure and a flowchart of the overall process are presented in Figure 1.

First, the rear structure was fabricated by the deposition of a thin silicon oxide layer on both sides of the wafers via oxidation using an H_2O_2 solution.[39] After the deposition of the oxide, 300-nm-thick polysilicon layers (poly-Si) were deposited on both sides via low-pressure chemical vapor deposition. In this step, two different types of poly-Si were used, namely, intrinsic (i-poly-Si) and in situ P-doped polysilicon (in situ P-doped poly-Si). In addition, $POCl_3$ diffusion was used to dope i-poly-Si and form an *n* + poly-Si/SiO_x structure. This sample is referred to as $POCl_3$-doped poly-Si. When carrying out $POCl_3$ diffusion, the annealing temperature and time at the drive-in step were controlled from 800°C to 950°C and from 10 to 60 minutes, respectively. The fixed predeposition step with $POCl_3$ and O_2 gas mixture was conducted at 740°C for 20 min. For the in situ P-doped poly-Si, only annealing in an N_2 atmosphere was carried out, without the predeposition step. The annealing temperature and time spent in the N_2 atmosphere were changed from 800°C to 950°C and from 10 to 60 minutes, respectively. After annealing, the samples were further passivated via a hydrogenation process by the deposition of silicon nitride (SiN_x) and aluminum oxide (Al_2O_3), using plasma-enhanced chemical vapor deposition (PECVD) and atomic layer deposition, respectively, with additional annealing via a rapid thermal process at 600°C for 15 min. The SiN_x/Al_2O_3 stack layers were removed by immersion in hydrofluoric acid (HF) after the hydrogenation. For the evaluation of the rear structure, the lifetime, sheet resistance, doping concentration profile, and grain-size map were obtained using quasi–steady-state photoconductance (Sinton WCT-100), the four-point probe (FPP) method (AIT CMT-100S), secondary ion mass spectroscopy (SIMS, Cameca IMS 4FE7), and high-resolution electron backscatter diffraction (EBSD) (Bruker) mapping, respectively, using an ultrahigh analytical field emission scanning electron microscope (SEM, Hitachi S-4800). Because silicon oxide formation and the polysilicon deposition process constitute a two-sided process, the sample is sandwich structured (ie, it has the structure of poly-Si/SiO_x/c-Si/SiO_x/poly-Si). Thus, to form the emitter, the front poly-Si/SiO_x layers and random pyramid texturing on the front surface are required. Before the etching of the poly-Si/SiO_x layers, we deposited a SiN_x barrier layer on the back surface using PECVD. Following the SiN_x deposition, the *n* + poly-Si layer was etched by TMAH solution and the SiO_x layer was etched by dipping it in diluted HF solution. After removing the front poly-Si/SiO_x layers, a random pyramid texture was formed on the front surface using KOH solution.

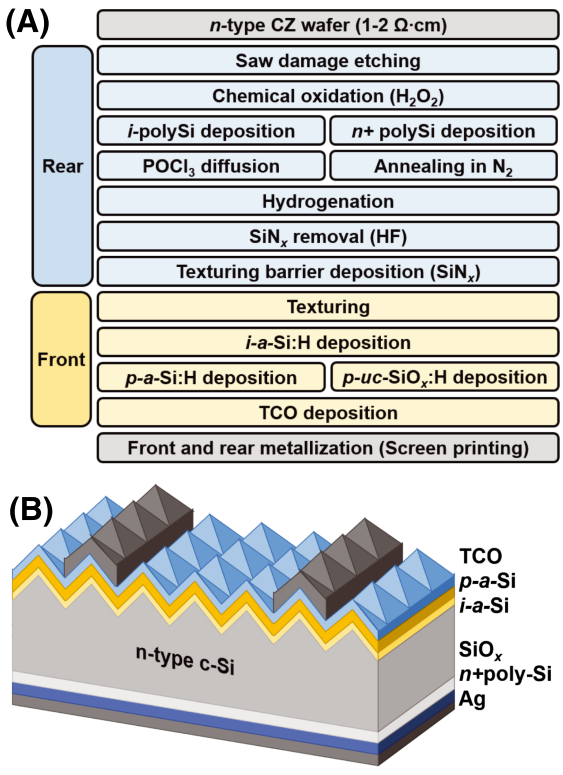

FIGURE 1 (A) Experimental procedure for fabrication of hybrid solar cell and (B) the final cell structure after the fabrication process [Colour figure can be viewed at wileyonlinelibrary.com]

After the front texturing, the amorphous layers were deposited in a multichamber PECVD system. A radiofrequency (RF) of 13.56 MHz was used for the p-type *a*-Si:H and p-type *μc*-SiO:H. In addition, a very high RF of 60 MHz was used for the intrinsic *a*-Si:H. Prior to the deposition, n-type wafers were immersed in HF immediately before loading into the multichamber PECVD system. The intrinsic *a*-Si:H and p-type *a*-Si:H layers were deposited on the front side of the wafer at 200°C using separate chambers. The thickness of the intrinsic *a*-Si:H layer was 7 nm, and that of the p-type *a*-Si:H layer was 10 nm. The gases commonly used for the deposition of intrinsic and p-type *a*-Si:H, silane (SiH_4), and hydrogen gases were employed. For p-type *μc*-SiO_x:H, an RF power density of 2.8 mW/cm^2, working pressure of 1.5 Torr, and electrode separation of 2.0 cm were used for a thickness of 35 nm at a deposition temperature of 100°C. For the deposition of *μc*-SiO_x:H, SiH_4, H_2, carbon dioxide (CO_2), and diborane (B_2H_6) gases were used at gas flow rates of 5 sccm (SiH_4), 0.003(+0.297) − 0.005 (+0.0495) sccm (B_2H_6(+H_2)), 5 sccm (CO_2), and 900 sccm (H_2). Although the CO_2 ratio according to the crystallinity of the layer is already reported, for fine tuning process, we varied the B_2H_6 (99%, diluted with hydrogen) flow rate from 2.0 to 0.3 sccm, which is one of the methods for the enhancement of the layer crystallinity.[40,41] With an increase in the crystallinity, there was an increase in the optical gap, and the electrical conductivity was improved. After the deposition of the p-type Si layer, an indium tin oxide (ITO) film was deposited at the front via RF sputtering at 200°C with a thickness of 80 nm using an ITO target (99.999% purity) composed of 90-wt% In_2O_3 and 10-wt% SnO_2. Finally, the hybrid cell was completed via

metallization by employing a silver metal grid with screen printing on the front side, and a full-area silver grid on the rear side using thermal evaporation. For the characterization of the front structure, the opto-electronic properties of the films were evaluated. Spectroscopic ellipsometry (SE, VASE, J. A. Woollam, 240 nm < λ < 1700 nm) was used to determine the thickness, refractive index, absorption coefficient, and optical bandgap at an angle of incidence of 65°, within the spectral range from 240 to 1700 nm. A Raman system (Dongwoo Optron) with a 514.5-nm Ar^+ ion laser line was used to estimate the microcrystalline phase fraction from multiple peaks with *a*-Si state, *μc*-Si grain boundary state, and c-Si state using peak positions of approximately 480, 500, and 520 cm^{-1} from the Raman transverse optical (TO) modes.[42,43] The crystallinity of the films, ie, the crystalline volume fraction, was estimated from the integration of the peaks at 480 cm^{-1} (I_{480}), 500 cm^{-1} (I_{500}), and 520 cm^{-1} (I_{520}) using Equation (1)

$$X_c = (I_{520} + I_{500})/(I_{520} + I_{500} + I_{480}). \quad (1)$$

The conductivity of the films was measured at a thickness of 50 nm using a programmable Keithley 617 electrometer. The activation energy (E_a) was determined from the temperature-dependent dark conductivity σ_d (*T*) using the Arrhenius relationship[44]:

$$\sigma_d\,(T) = \sigma_o \exp\,(-E_a/kT), \quad (2)$$

where σ_o is the conductivity prefactor, *T* is the absolute temperature, and *k* is the Boltzmann's constant. Furthermore, the surface passivation quality was determined using a Sinton WCT-120 lifetime tester. Here, the implied open-circuit voltage (iV_{OC}) at 1 sun was used as a factor to evaluate the surface passivation quality. The hybrid cells were characterized by obtaining current density–voltage curves under AM 1.5 illumination with a light intensity of 100 mW/cm^2 at 25°C. The quantum efficiency (QE) of the hybrid cells was determined using an external QE (EQE) and internal QE (IQE) system (PV measurement Inc., QEX7).

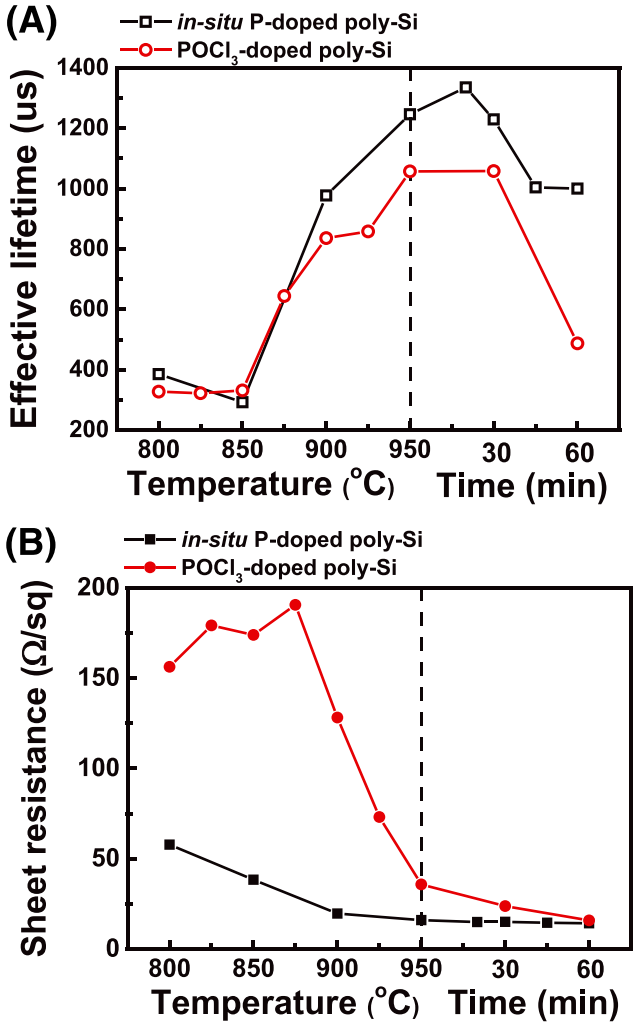

FIGURE 2 (A) Effective lifetime and (B) sheet resistance of in situ P-doped poly-Si and $POCl_3$-doped poly-Si (the lifetimes were determined using quasi–steady-state photoconductivity [QSSPC] at an intensity of 1 sun) [Colour figure can be viewed at wileyonlinelibrary.com]

3 | RESULTS AND DISCUSSION

3.1 | Rear structure

To improve the passivation and contact quality, the annealing temperature and time were varied. The experimental results are presented in Figure 2. The increase in the annealing temperature improved the lifetime. In particular, the lifetime of $POCl_3$-doped poly-Si increased from 327 to 1057 μs, and that of in situ P-doped poly-Si increased from 385 to 1246 μs. The increase in the lifetime and passivation quality due to high-temperature annealing may be because of the improved passivation quality of the interfacial oxide, given that the density of the interface defect of the oxide layer decreases in accordance with an increase in the annealing temperature.[45] Another possible cause of the increased lifetime is the grain-size growth, given that the grain boundary area induces recombination.[46,47] An increase in the annealing time and temperature may result in a gettering effect,[7] given that impurity defects are gettered at the poly-Si layer. In addition, increasing the annealing temperature affected the sheet resistance, as shown in Figure 2B, which means that the increased lifetime can also be affected by a change of the doping concentration profile, because the doping concentration at poly-Si and c-Si determines the tunneling current and carrier selectivity.[48] However, upon a further increase in the annealing time, the lifetimes of both $POCl_3$-doped poly-Si and in situ P-doped poly-Si decreased. Thus, in this study, the factors responsible for changes in the passivation quality with respect to the annealing temperature, time, and doping method were analyzed using SIMS, to obtain the doping profile; and EBSD was used for grain-size analysis.

Figure 3 presents the SIMS measurement results for the doping concentration profile of phosphorus and the intensity of oxygen along the depth direction. As shown in Figure 3, the in-diffusion of phosphorus increased in accordance with an increase in the annealing time for both poly-Si passivating contacts. This indicates that the deterioration

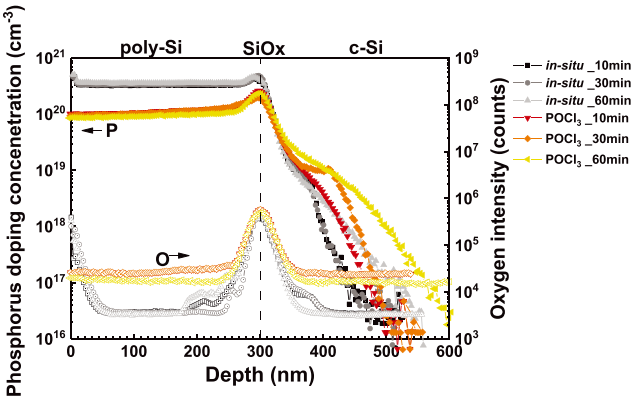

FIGURE 3 Phosphorus doping concentration and oxygen intensity profile with respect to the depth obtained via secondary ion mass spectroscopy (SIMS) [Colour figure can be viewed at wileyonlinelibrary.com]

of the lifetime could be due to the phosphorus in-diffusion into substrate.[47-51] In addition, when compared with the $POCl_3$-doped poly-Si and in situ P-doped poly-Si, the in situ P-doped poly-Si exhibited a lower in-diffusion and higher doping concentration within the poly-Si layer. This may be due to the different doping methods employed. Moreover, the $POCl_3$ diffusion formed a phosphor-silicate glass layer with a high doping concentration[52] of approximately 10^{21} cm^{-3}, which could increase the phosphorus in-diffusion when compared with in situ P-doped poly-Si, given that the dopant dose was limited at the step of poly-Si layer deposition.

In addition to the evaluation of the in-diffusion effect, each grain was analyzed by determining the grain size and its orientation using EBSD. Figure 4 presents a comparison of the EBSD images of the $POCl_3$-diffused and in situ P-doped poly-Si samples after annealing and hydrogenation. In Figure 4, the EBSD image shows $POCl_3$-doped poly-Si annealed at 950°C for 20 min and in situ P-doped poly-Si at 950°C for 30 min, which are the annealing conditions for the highest lifetime in Figure 2A. Prior to annealing, the grains of poly-Si were not detectable from the EBSD image, given that the grain size was excessively small. The grain size prior to the annealing process was expected to be on the scale of approximately 10 nm.[46] After annealing, the grain size of poly-Si increased to the 0.1- to 1-μm scale. Hence, the grain size was increased by annealing, which indicates that the increase in the grain size of the poly-Si layer may have an influence on the increase in the lifetime, due to the reduced recombination at the grain boundary region.[47] In addition, because the recombination is critically affected by the silicon oxide layer and, as shown in recent research, this layer does not allow the recombination from bulk to grain, the increased lifetime may be caused by improvement of the silicon oxide layer.[53-55] From a comparison of the $POCl_3$-doped poly-Si and in situ P-doped poly-Si, it was found that the in situ P-doped poly-Si had a larger grain size after annealing. This indicates that the in situ P-doped poly-Si can achieve a higher passivation quality than the $POCl_3$-doped poly-Si, due to the larger grain size with low in-diffusion and a higher doping concentration, which improves the passivation quality and contact property.

3.2 | Front structure

To reduce the parasitic absorption in the emitter layers, wide-bandgap *μc*-SiO:H films were employed. In particular, p-type *a*-Si:H and *μc*-SiO:H films with different bandgaps were used as the front emitter. The optical and electrical properties of each emitter layer were analyzed. The optical bandgaps (E_{opt}) of the p-type *a*-Si:H and *μc*-SiO:H films are presented in Figure 5A. The optical absorption coefficients of the films were determined using SE, and $(\alpha h\nu)^{1/2}$ was plotted as a function of $h\nu$, thus yielding a Tauc plot. The E_{opt} of the p-type *μc*-SiO:H films was determined to be within the range of 2.13 to 2.33 eV, whereas

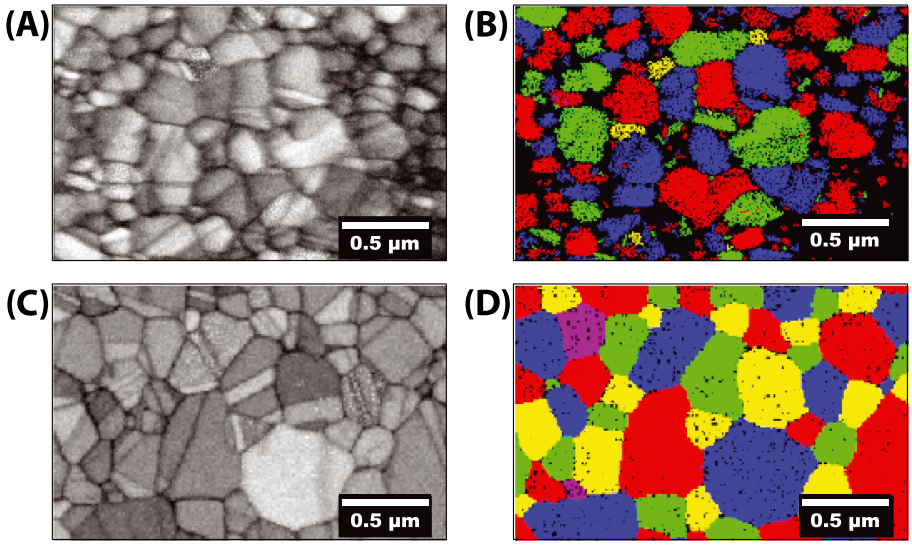

FIGURE 4 Electron backscatter diffraction (EBSD) pattern-quality map and grain maps of (A,B) $POCl_3$-diffused poly-Si and (C,D) in situ P-doped poly-Si, respectively (color in the grain map is random and only displays different grains) [Colour figure can be viewed at wileyonlinelibrary.com]

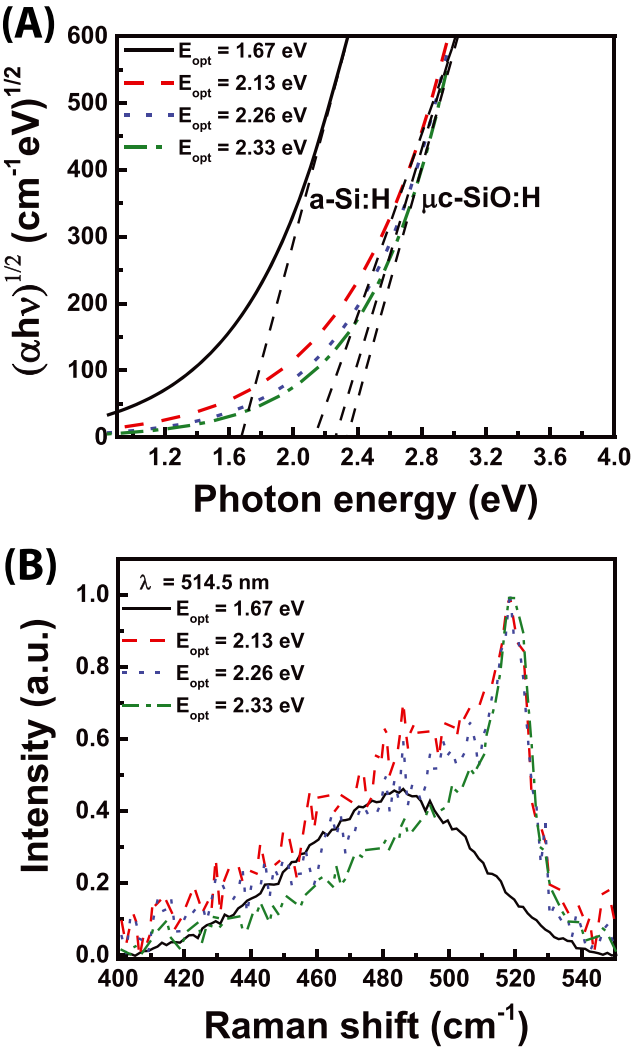

FIGURE 5 (A) Optical bandgap (E_{opt}) of p-type *a*-Si:H and p-type *μc*-SiO:H films (E_{opt} was determined using the Tauc plot) and (B) the crystallinity of the wide-bandgap p-type *μc*-SiO:H film with different values of E_{opt} [Colour figure can be viewed at wileyonlinelibrary.com]

that of boron-doped p-type *a*-Si:H was 1.67 eV. The X_c values of the p-type *a*-Si:H and p-type *μc*-SiO:H films were determined from the Raman spectra, as shown in Figure 5B. The focal depth of the 514.5-nm laser (Ar^+) ranged from tens to hundreds of nanometers, and the inverse of the absorption coefficient of the p-type *a*-Si:H or p-type *μc*-SiO:H film was 514.5 nm. The crystallinity of the 50-nm-thick layers was evaluated. Moreover, the film with a bandgap of 1.67 eV exhibited a dominant 480-cm^{-1} peak, and the film with a bandgap of 2.33 eV exhibited a dominant 520-cm^{-1} peak. With an increase in the bandgap, there was a decrease in the mixed-phase peak at 500 cm^{-1}. The phase information was obtained from the TO mode according to Figure 5B, and the X_c values of the films were estimated using Equation (1). Furthermore, X_c was found to increase with values of 40.20%, 42.93%, and 45.15% in accordance with an increase in E_{opt} of the p-type emitter layer, with values of 2.13, 2.26, and 2.33 eV (see Table 1). The films prepared with lower doping ratios and higher hydrogen dilution ratios exhibited higher optical gaps (E_{opt}) with high

TABLE 1 Bandgap, activation energy, dark conductivity, and crystallinity of the p-type *a*-Si:H and p-type *μc*-SiO:H films with different values of E_{opt}

p-Type Emitter	E_g, eV	E_a, eV	σ_d, S/cm	X_c, %
a-Si:H (50 nm)	E_{opt} 1.67	0.323	1.65×10^{-04}	0
μc-SiO_x:H (50 nm)	E_{opt} 2.13	0.091	1.53×10^{-02}	40.20
	E_{opt} 2.26	0.098	1.26×10^{-02}	42.93
	E_{opt} 2.33	0.113	9.95×10^{-03}	45.15

dark conductivities (σ_d) and lower activation energies (E_a). Additional details are covered in the following X-ray photoelectron spectroscopy (XPS) results. It should be noted that all the p-type *μc*-SiO:H films exhibited better properties than the p-type *a*-Si:H films (see Table 1).

A trend was found during the analysis of the iV_{OC} results (Figure 6 A) for the samples deposited with p-type *a*-Si:H and *μc*-SiO:H before ITO deposition. The samples with p-type *μc*-SiO:H had an iV_{OC} value approximately 10-mV higher than that of the *a*-Si:H samples, and the lifetimes were approximately 1 ms longer. This was considered as a naturally occurring effect of the hydrogen plasma treatment, given

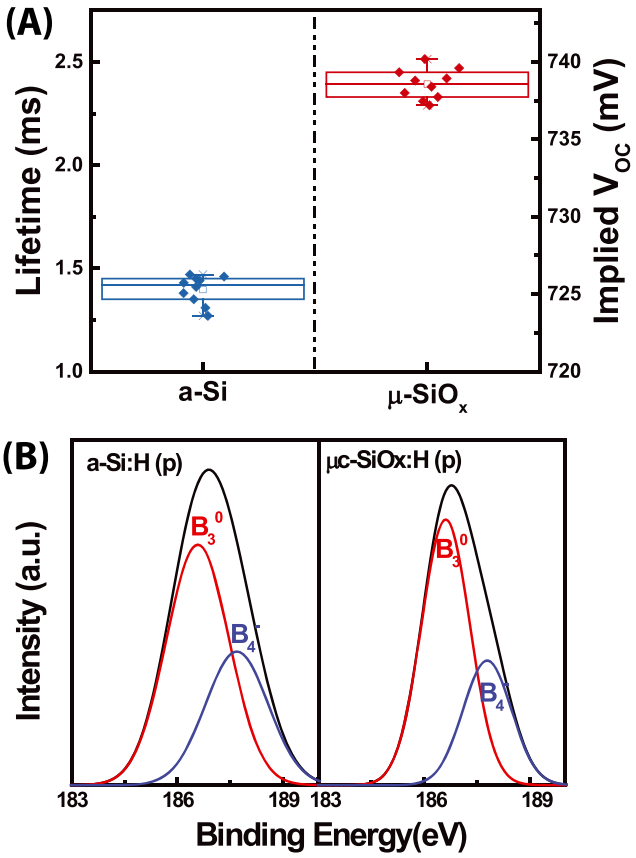

FIGURE 6 (A) Implied V_{OC} value and minority carrier lifetime of a p-type *a*-Si:H (blue circle) emitter and a *μc*-SiO:H (red triangle) emitter and (B) the deconvolution of the B 1s XPS spectra of p-type *a*-Si:H (left) and *μc*-SiO:H films (right). The peak at 186.6 eV can be attributed to the threefold coordination of B atoms (red line), and that at 187.7 eV can be attributed to the fourfold coordination of B atoms (blue line) [Colour figure can be viewed at wileyonlinelibrary.com]

that the hydrogen flow rate during the deposition for microcrystalline formation was higher than that of *a*-Si:H by a factor of 10.[56,57] There was a clear increase in the hydrogen content of the p-type *μc*-SiO:H films, as verified using infrared spectroscopy, given that the total area under the Si-H and Si-H_2 peaks (2000 and 2090 cm^{-1}, respectively) for these films was larger than that for the p-type *a*-Si:H films (not shown).[58,59] XPS was conducted on the p-type *μc*-SiO:H films to obtain additional information on the atomic bonding configurations. The peak at 186.6 eV can be attributed to threefold coordinated boron (B) atoms (B_3^0), and that at 187.7 eV can be attributed to the fourfold coordination of B atoms (B_4^-) in the form of Si-B.[60] The results of the deconvolution analysis, assuming a Gaussian function (see Figure 6B), revealed the state of the boron component in the p-type *a*-Si:H and *μc*-SiO:H films. The peak of B_3^0 is related to inactive B atoms, which act like impurities (defects); and the peak of B_4^- is related to active B atoms, which are related to the dark conductivity (σ_d).[61] The p-type *μc*-SiO:H films had relatively low overall Si-B bonds and lower-intensity B_4^- peaks than the *a*-Si:H films; however, their conductivity was one order of magnitude higher. For example, certain boron atoms incorporated in the p-type *μc*-SiO:H films formed B-Si-H bonds by consuming atomic H. This reduced the coverage of the growing surface by atomic H, which was necessary for the microcrystalline phase formation in the surface diffusion model.[62] This is because the microcrystalline phase in the p-type *μc*-SiO:H films contribute significantly to the transfer of carriers. In particular, in conjunction with the microcrystalline phase, a high conductivity can be obtained with a small amount of doping gas.[63-65] This analysis can also explain the iV_{OC} results presented previously. Boron has a less significant influence on the p-type *μc*-SiO:H films when the hydrogen treatment effect is not considered.

3.3 | Evaluation of hybrid cell

3.3.1 | Cell result

The QE results of the hybrid solar cell are presented in Figure 7. The results of the short-wavelength region (300-600 nm) are presented to confirm the behavior of the emitter layer. With an increase in the optical bandgap of the emitter layer, the QE at shorter wavelengths gradually increased. The improvement of the EQE in the short-wavelength range of 300 to 500 nm was significant (Figure 7A), and the improvement of the IQE (Figure 7B) was found to be in the range of 300 to 600 nm. The short wavelength enhancement in EQE results from the reduction of parasitic optical loss due to the high band gap and low doping concentration of the *μc*-SiO:H emitter. In addition, the improvement in IQE results from the reduced carrier recombination arising from the excellent electrical properties of the *μc*-SiO:H emitter. These EQE and IQE results reveal that the developed p-type *μc*-SiO:H emitters are optically and electrically superior to the *a*-Si:H emitters.

Based on the QE results, the solar cell current density (J_{sc}) also increased in accordance with an increase in the emitter bandgap, whereas the fill factor (FF) of the hybrid cells exhibited a different trend (Figure 8). All the hybrid solar cells with p-type *μc*-SiO:H

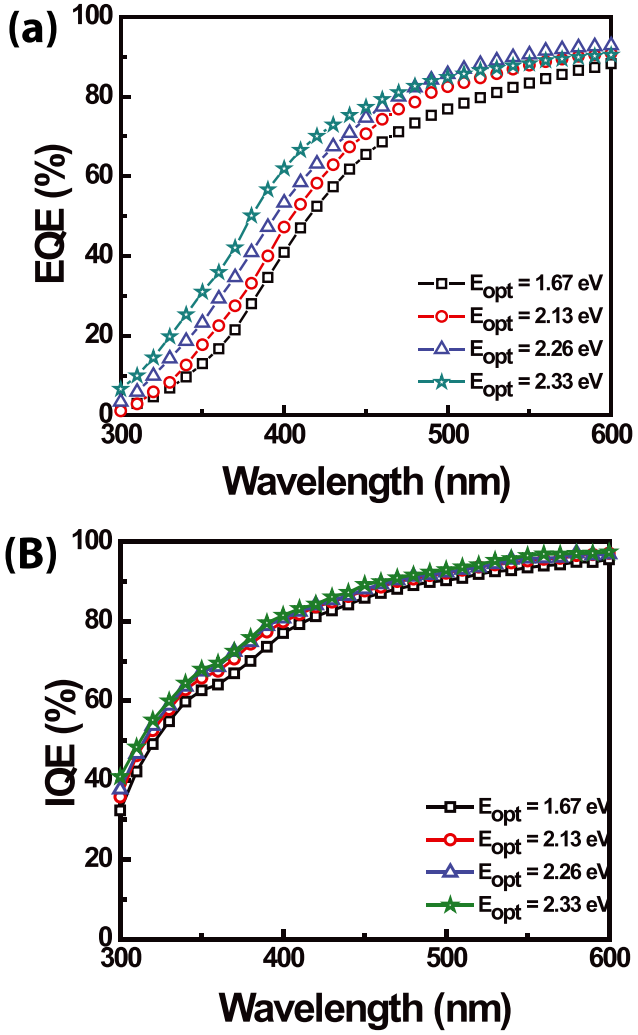

FIGURE 7 (A) Short-wavelength region of the EQE as a function of the wavelength for the hybrid cells with p-type *a*-Si:H and *μc*-SiO:H emitters of different bandgaps and (B) the short-wavelength region of the IQE as a function of the wavelength for the same hybrid cells [Colour figure can be viewed at wileyonlinelibrary.com]

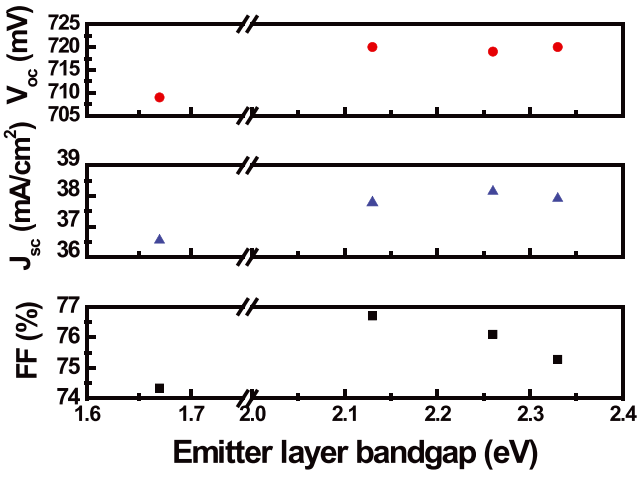

FIGURE 8 Fill factor (FF) (bottom, black square), current density J_{sc} (middle, blue triangle), and open-circuit voltage V_{OC} (top, red circle) of hybrid solar cells with different bandgap emitter layers [Colour figure can be viewed at wileyonlinelibrary.com]

emitters had an improved FF when compared with those with an *a*-Si:H emitter. Unlike the gradual increase in J_{sc}, the μc-SiO:H emitter with a bandgap of 2.13 eV exhibited the highest FF of 76.7%. Moreover, the emitters with bandgaps of 2.26 and 2.33 eV exhibited FFs of 76.1% and 75.3%, respectively. The pronounced decrease in FF can be attributed to the decrease in the corresponding σ_d (Table 1). The conductivity of the p-type μc-SiO_x:H thin film with a band gap of 2.33 eV is lower than that of the other p-type μc-SiO_x:H. Therefore, it is reasonable that the FF of the cell with an emitter having E_{opt} of 2.33 eV is low, even in the solar cell results. Figure 8 also reveals that the effect of the hydrogen plasma treatment (shown in Figure 6A) improves the V_{OC} in the real device. Experiments (Figures 7 and 8) were conducted on the rear side of the in situ P-doped poly-Si structure using variable emitters.

The results of the current-voltage (*I*-*V*) measurements under illumination are presented in Table 2. Three types of the hybrid cells could be analyzed. Cell types A and B have the same rear side structure and different front emitters (p-type *a*-Si:H and μc-SiO:H), and cell types B and C have the same front structure (p-type μc-SiO:H with E_{opt} of 2.26 eV) and differently processed rear structures ($POCl_3$-diffused and in situ P-doped poly-Si). The V_{OC} increased from 705 to 710 mV, the J_{sc} increased from 36.55 to 37.64 mA/cm^2, and the FF increased from 74.51% to 76.72% upon the application of a μc-SiO_x:H emitter instead of *a*-Si:H. Improvements in all parameters of the solar cell demonstrate the excellent performance of the applied μc-SiO_x:H. A higher V_{OC} and efficiency were achieved by applying the in situ P-doped poly-Si, which can be attributed to the higher passivation quality with a low sheet resistance. By changing the front metal design, a high efficiency of 21.8% with a V_{OC} of 715 mV, J_{SC} of 40.9 mA/cm^2, and an FF of 74.7% was achieved for a cell area of 4 cm^2.

Approach to improve the cell efficiency of hybrid

To investigate the efficiency limit of the hybrid solar cell, a simulation was conducted using the QUOKKA2[66] and OPAL 2[67] program. To identify the difference between heterojunction and poly-Si passivated contact, the absorption characteristics were included in the J_{SC} simulation using OPAL2 because amorphous silicon and polycrystalline silicon layers have different absorption coefficients. For the cell efficiency simulation using QUOKKA2, the input parameters are listed in Table 3. First, the hybrid cell was simulated using parameters based on measurement data obtained from the experimental results. This simulation result was denoted as "real cell," as presented in Table 3. The bulk properties (wafer resistivity, thickness, and bulk lifetime) were measured using FPP, a Vernier caliper, and quasi–steady-state photoconductivity (QSSPC), respectively. The other properties, which include the sheet resistance, recombination current density, and contact resistance at the front and rear were measured using FPP, QSSPC, and the transmission line measurement (TLM) method. As a result, the simulated real cell efficiency was 22.8%, which was 1% higher than that of the actualized hybrid cell. The differences could be due to the uniformity of the front and rear passivation layers, as the lower efficiency was confirmed for the large cell area (4 cm^2 for 21.8%, and 10.24 cm^2 for 21.1%). The V_{OC} from the simulation was almost the same as cell result C in Table 2, which indicates that the recombination from the metallization was minimally affected, given that ITO and low-temperature firing paste were used for the front metallization. In addition, the simulated real-cell result indicates that J_{SC} was in good agreement with the cell result after the adjustment of the front metal design. This indicates that the potential of J_{SC} using the hybrid structure was realized in this study using a different front metal design. Finally, the FF of the simulated real cell was 77.4%, which was close to and slightly higher than the fabricated cell result C of 76.9%. Finally,

TABLE 3 Input parameters of hybrid cell simulation

Parameter		Unit	Real Cell	Optimized Cell
Bulk	Resistivity	Ω·cm	1	0.1-10
	Thickness	μm	190	80-200
	Lifetime	μs	2,360	2.00E + 04
Front	Sheet resistance	Ω/sq	35	35
	Recombination current density	A/cm^2	1.19E-14	1.00E − 15
	Contact resistance	mΩ·cm	19	0.1
Rear	Sheet resistance	Ω/sq	15	15
	Recombination current density	A/cm^2	0.43E-14	1.00E − 5
	Contact resistance	mΩ·cm	25	0.1
Contact	Finger width	μm	50	50
	Finger pitch	μm	1395	1395
Generation	Current density	mA/cm^2	40.6	40.6

Note. According to the measurement values, the input parameters were based on the measurement result. By adjusting the input parameters, which included the bulk properties such as the lifetime, resistivity and thickness, contact resistance, and recombination current density; a simulated maximum efficiency of 26% was achieved. Moreover, the simulation parameters for the previously mentioned cell are presented in the table (denoted as "optimized cell").

TABLE 2 *I*-*V* results for hybrid cells

Hybrid Cell Type	V_{OC}, mV	J_{sc}, mA/cm^2	FF, %	*n*, %
A—F: *a*-Si:H/R: $POCl_3$	705	36.55	74.51	19.20
B—F: μc-SiO_x:H/R: $POCl_3$	710	37.64	76.72	20.51
C—F: μc-SiO_x:H/R: P in situ	719	38.15	76.91	21.10

Note. Cell type A is composed of a p-type *a*-Si:H emitter at the front and $POCl_3$-diffused poly-Si in the rear side. Cell type B is composed of a p-type μc-SiO:H emitter and $POCl_3$-diffused poly-Si. Cell type C is composed of a p-type μc-SiO:H emitter and in situ P-doped poly-Si.

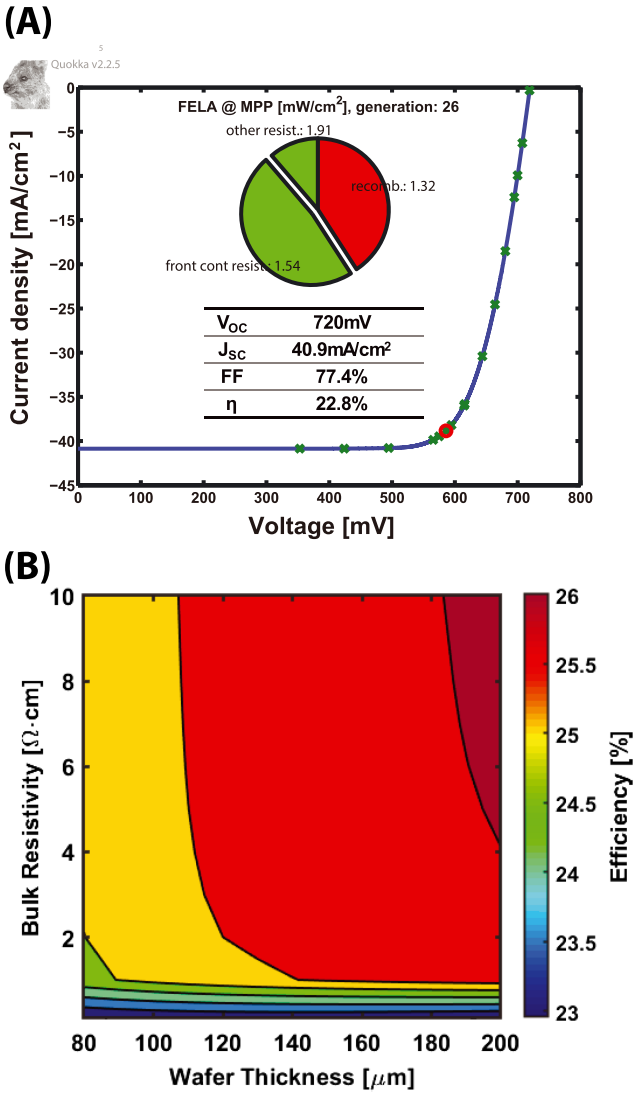

FIGURE 9 Hybrid cell simulation results obtained using the QUOKKA2 program [Colour figure can be viewed at wileyonlinelibrary.com]

the potential efficiency limit of the hybrid cell was evaluated by adjusting the parameters, thus yielding the optimized cell in Table 3. The resulting efficiency was 26%, as shown in Figure 9. The simulation results indicate that to achieve an efficiency of 26% using the hybrid structure, an n-type silicon wafer with a resistivity greater than 5 Ω·cm and thickness greater than 180 μm is required with further improvements in the passivation quality and contact quality. The simulation results also reveal that the recombination current density at the front and rear should be approximately 1 fA/cm^2, and the contact resistance should be 0.1 mΩ·cm, to achieve a solar cell efficiency of 26%, which indicates the direction of future development with respect to the cell structure.

4 | SUMMARY

A hybrid silicon solar cell referred to as hybrid, which had a high efficiency of 21.8%, was evaluated. For the fabrication of the hybrid cell, the rear polysilicon passivating contact structure was first constructed. The rear structure was evaluated with respect to the lifetime and sheet resistance using two different formation methods for *n* + poly-Si, with a variation in the annealing temperature and time. In this study, all the poly-Si passivating contacts underwent the hydrogenation process to increase the lifetime. Consequently, the in situ P-doped poly-Si passivating contact exhibited a longer lifetime with a lower sheet resistance due to the larger grain size and suppressed phosphorus in-diffusion, when compared with the $POCl_3$-doped poly-Si. After the formation of the rear structure, the front structure was formed with intrinsic thin amorphous Si and p-type Si layers deposited via PECVD. For the p-type Si layer, the crystallinity was controlled, and two different Si layers were evaluated: *a*-Si:H and *μc*-SiO:H. With an increase in the crystallinity of *μc*-SiO:H, a higher passivation quality with a high conductivity and low bandgap energy can be achieved. Finally, the hybrid cell results revealed that hybrid with *μc*-SiO:H at the front interface layer, in addition to in situ P-doped poly-Si at the rear, exhibited the highest efficiency of 21.1% for an area of 10.24 cm^2. In additional, with the improved front metal design, the cell efficiency increased to 21.8% for an area of 4 cm^2. Finally, the efficiency limit of the hybrid cell was simulated using the QUOKKA2 simulation program. The simulation results revealed that an efficiency of 26% could be achieved by improving the front and rear passivation quality, in addition to the contact resistance, using a long-lifetime wafer.

ACKNOWLEDGEMENTS

This research was supported by the New & Renewable Energy Core Technology Program of the Korea Institute of Energy Technology Evaluation and Planning (KETEP), with financial support from the Ministry of Trade, Industry & Energy, Republic of Korea (no. 20163030014020), and the Technology Development Program to Solve Climate Changes of the National Research Foundation (NRF) funded by the Ministry of Science and ICT (NRF-2017M1A2A2087351). This work was supported by the "Human Resources Program in Energy Technology" of the Korea Institute of Energy Technology Evaluation and Planning (KETEP), with financial support from the Ministry of Trade, Industry and Energy, Republic of Korea (no. 20154030200760).

ORCID

HyunJung Park https://orcid.org/0000-0001-9008-0224

REFERENCES

1. Wurfel U, Cuevas A, Wurfel P. Charge carrier separation in solar cells. *IEEE J Photovoltaics*. 2015;5(1):461-469.
2. Battaglia C, Cuevas A, De Wolf S. High-efficiency crystalline silicon solar cells: status and perspectives. *Energ Environ Sci*. 2016;9(5):1552-1576.
3. Melskens J, Kessels WMM, Black LE, van de Loo BWH, Macco B, Smit S. Passivating Contacts for crystalline silicon solar cells: from concepts and materials to prospects. *IEEE J Photovoltaics*. 2018;8(2):373-388.

4. Feldmann F, Nogay G, Polzin JI, et al. A study on the charge carrier transport of passivating contacts. *IEEE J Photovoltaics*. 2018;8(6): 1503-1509.
5. Feldmann F, Bivour M, Reichel C, Hermle M, Glunz SW. Passivated rear contacts for high-efficiency n-type Si solar cells providing high interface passivation quality and excellent transport characteristics. *Sol Energy Mater Sol Cells*. 2014;120, no. PART A:270-274.
6. Römer U, Peibst R, Ohrdes T, et al. Recombination behavior and contact resistance of n+ and p+ poly-crystalline Si/mono-crystalline Si junctions. *Sol Energy Mater Sol Cells*. 2014;131:85-91.
7. Liu AY, Yan D, Phang SP, Cuevas A, Macdonald D. Effective impurity gettering by phosphorus- and boron-diffused polysilicon passivating contacts for silicon solar cells. *Sol Energy Mater Sol Cells*. 2018;179:136-141.
8. Yan D, Cuevas A, Bullock J, Wan Y, Samundsett C. Phosphorus-diffused polysilicon contacts for solar cells. *Sol Energy Mater Sol Cells*. 2015;142:75-82.
9. Yoshikawa K, Kawasaki H, Yoshida W, et al. Silicon heterojunction solar cell with interdigitated back contacts for a photoconversion efficiency over 26%. *Nat Energy*. 2017;2(5):17032.
10. Green MA, Hishikawa Y, Dunlop ED, et al. Solar cell efficiency tables (Version 53). *Prog Photovoltaics Res Appl*. 2019;27(1):3-12.
11. Taguchi M, Yano A, Tohoda S, et al. 24.7% Record efficiency HIT solar cell on thin silicon wafer. *IEEE J Photovoltaics*. 2014;4(1):96-99.
12. Scheer HC. The influence of the amorphous silicon deposition temperature on the ITO/a-Si:H/c-Si heterojunction solar cells and properties of interfaces. *Thin Solid Films*. 2002;403–404:359-362.
13. Maydell KV, Conrad E, Schmidt M. Efficient silicon heterojunction solar cells based on p- and n-type substrates processed at temperatures <220°C. *Prog Photovoltaics Res Appl*. 2006;14(4): 289-295.
14. Wang Q, Wang TH, Iwaniczko E, et al. Effect of emitter deposition temperature on surface passivation in hot-wire chemical vapor deposited silicon heterojunction solar cells. *Thin Solid Films*. 2005;501(1–2):284-287.
15. Jeon M, Yoshiba S, Kamisako K. Hydrogenated amorphous silicon film as intrinsic passivation layer deposited at various temperatures using RF remote-PECVD technique. *Curr Appl Phys*. 2010;10(2 SUPPL): S237-S240.
16. Lee Y, Han S, Kim S, et al. Performance of hetero junction with intrinsic thin-layer solar cell depending upon contact resistivity of front electrode. *J Photonics Energy*. 2014;4(1):043094.
17. Feldmann F, Bivour M, Reichel C, Steinkemper H, Hermle M, Glunz SW. Tunnel oxide passivated contacts as an alternative to partial rear contacts. *Sol Energy Mater Sol Cells*. 2014;131:46-50.
18. Matsushita T, Oh-Uchi N, Hayashi H, Yamoto H. A silicon heterojunction transistor. *Appl Phys Lett*. 1979;35(7):549-550.
19. Yablonovitch E, Gmitter T, Swanson RM, Kwark YH. A 720 mV open circuit voltage SiO_x:c-Si:SiO_x double heterostructure solar cell. *Appl Phys Lett*. 1985;47(11):1211-1213.
20. Garcia-Alonso D, Smit S, Bordihn S, Kessels WMM. Silicon passivation and tunneling contact formation by atomic layer deposited Al2O3/ZnO stacks. *Semicond Sci Technol*. 2013;28(8):082002.
21. Rohatgi A, Rounsaville B, Ok YW, et al. Fabrication and modeling of high-efficiency front junction n-type silicon solar cells with tunnel oxide passivating back contact. *IEEE J Photovoltaics*. 2017;7(5): 1236-1243.
22. Wietler TF, Tetzlaff D, Krügener J, et al. Pinhole density and contact resistivity of carrier selective junctions with polycrystalline silicon on oxide. *Appl Phys Lett*. 2017;110(25):5.
23. Haase F, Hollemann C, Schäfer S, et al. Laser contact openings for local poly-Si-metal contacts enabling 26.1%-efficient POLO-IBC solar cells. *Sol Energy Mater Sol Cells*. 2018;186, no. March:184-193.
24. Richter A, Benick J, Feldmann F, Fell A, Hermle M, Glunz SW. n-Type Si solar cells with passivating electron contact: identifying sources for efficiency limitations by wafer thickness and resistivity variation. *Sol Energy Mater Sol Cells*. 2017;173:96-105.
25. Lago R, PÃ©rez L, Kerp H, et al. Screen printing metallization of boron emitters. *Prog Photovoltaics Res Appl*. 2010;18(1):20-27.
26. Riegel S, Mutter F, Hahn G, Terheiden B. Influence of the dopant on the contact formation to p+-type silicon. *Energy Procedia*. 2011;8:533-539.
27. Fritz S, Riegel S, Gloger S, et al. Influence of emitter properties on contact formation to p+ silicon. *Energy Procedia*. 2013;38:720-724.
28. Körner S, Kiefer F, Peibst R, Heinemeyer F, Krügener J, Eberstein M. Basic study on the influence of glass composition and aluminum content on the Ag/Al paste contact formation to boron emitters. *Energy Procedia*. 2015;67:20-30.
29. Feldmann F, Steinhauser B, Arya V, et al. Evaluation of TOPCon technology on large area solar cells. *33rd European Photovoltaic Solar Energy Conference and Exhibition (EU-PVSEC)*. Amsterdam, The Netherlands; 2017.
30. Ryu K, Cho E, Rohatgi A, Ok Y-W. Process development and comparison of various boron emitter technologies for high-efficiency (~21%) n-type silicon solar cells. *Prog Photovoltaics Res Appl*. Aug. 2016;24(8):1109-1115.
31. Schiele Y, Hahn G, Terheiden B. Contacting and recombination analysis of boron emitters via etch-back for advanced n-type Si solar cells. *29th Eur Photovolt Sol Energy Conf Exhib*. 2014;29, September:825-829.
32. Xu M, Bearda T, Filipič M, et al. Simple emitter patterning of silicon heterojunction interdigitated back-contact solar cells using damage-free laser ablation. *Sol Energy Mater Sol Cells*. 2018;186, no. March:78-83.
33. Limodio G, Yang G, Ge H, et al. Front and rear contact Si solar cells combining high and low thermal budget Si passivating contacts. *Sol Energy Mater Sol Cells*. 2019;194:28-35.
34. De Wolf S, Descoeudres A, Holman ZC, Ballif C. High-efficiency silicon heterojunction solar cells: a review. *Green*. 2012;2(1):7-24.
35. Feldmann F, Reichel C, Müller R, Hermle M. The application of poly-Si/SiO_x contacts as passivated top/rear contacts in Si solar cells. *Sol Energy Mater Sol Cells*. 2017;159:265-271.
36. Sritharathikhun J, Jiang F, Miyajima S, Yamada A, Konagai M. Optimization of p-type hydrogenated microcrystalline silicon oxide window layer for high-efficiency crystalline silicon heterojunction solar cells. *Jpn J Appl Phys*. 2009;48(10 Part 1):1016031–1016035.
37. Kirner S, Mazzarella L, Korte L, Stannowski B, Rech B, Schlatmann R. Silicon heterojunction solar cells with nanocrystalline silicon oxide emitter: insights into charge carrier transport. *IEEE J Photovoltaics*. 2015;5(6):1601-1605.
38. Ding K, Aeberhard U, Finger F, Rau U. Optimized amorphous silicon oxide buffer layers for silicon heterojunction solar cells with microcrystalline silicon oxide contact layers. *J Appl Phys*. 2013;113(13): 134501.
39. Kim H, Bae S, Ji KS, et al. Passivation properties of tunnel oxide layer in passivated contact silicon solar cells. *Appl Surf Sci*. 2017;409:140-148.
40. Ding K, Aeberhard U, Smirnov V, Holländer B, Finger F, Rau U. Wide gap microcrystalline silicon oxide emitter for a-SiO x:H/c-Si heterojunction solar cells. *Jpn J Appl Phys*. 2013;52(12):122304.
41. Ling ZP. "Design, fabrication and characterization of thin-film materials for heterojunction silicon wafer solar cells." PhD Thesis, National University of Singapore. 2014.

42. Han D, Lorentzen JD, Weinberg-Wolf J, McNeil LE, Wang Q. Raman study of thin films of amorphous-to-microcrystalline silicon prepared by hot- wire chemical vapor deposition Raman study of thin films of amorphous-to-microcrystalline silicon prepared by hot-wire chemical vapor deposition. *J Appl Phys*. 2003;2930(5):2930-2936.
43. Lyon SA, Nemanich RJ. Raman scattering from hydrogenated amorphous silicon. *Phys B + C*. 1983;117–118(2):871-873.
44. Kokorowski SA, Olson GL, Hess LD. Kinetics of laser-induced solid phase epitaxy in amorphous silicon films. *J Appl Phys*. Feb. 1982;53(2):921-926.
45. Deal BE, Sklar M, Grove AS, Snow EH. Characteristics of the surface-state charge (Qss) of Thermally Oxidized Silicon. *J Electrochem Soc*. 1967;114, no. d(3):266.
46. Harbeke G, Krausbauer L, Steigmeier EF, Widmer AE, Kappert HF, Neugebauer G. Growth and physical properties of LPCVD polycrystalline silicon films. *J Electrochem Soc*. 1984;131(3):675.
47. Park H, Park SJ, Bae S, et al. Passivation quality control in poly-Si/SiO_x/c-Si passivated contact solar cells with 734 mV implied open circuit voltage. *Sol Energy Mater Sol Cells*. 2018;189:21-26.
48. Steinkemper H, Feldmann F, Bivour M, Hermle M. Numerical simulation of carrier-selective electron contacts featuring tunnel oxides. *IEEE J Photovoltaics*. 2015;5(5):1348-1356.
49. Lancaster K, Großer S, Feldmann F, Naumann V, Hagendorf C. Study of pinhole conductivity at passivated carrier-selected contacts of silicon solar cells. *Energy Procedia*. 2016;92:116-121.
50. Tetzlaff D, Krügener J, Larionova Y, et al. A simple method for pinhole detection in carrier selective POLO-junctions for high efficiency silicon solar cells. *Sol Energy Mater Sol Cells*. 2017;173:106-110.
51. Tetzlaff D, Krügener J, Larionova Y, et al. Evolution of oxide disruptions: the (W)hole story about poly-Si/c-Si passivating contacts. *IEEE 43th Photovol Special Conf (PVSC)*. 2016;2:2-5.
52. Chen R, Wagner H, Dastgheib-Shirazi A, et al. A model for phosphosilicate glass deposition via POCl3 for control of phosphorus dose in Si. *J Appl Phys*. 2012;112(12):124912.
53. Choi S, Min KH, Jeong MS, et al. Structural evolution of tunneling oxide passivating contact upon thermal annealing. *Sci Rep*. 2017;7(1):1-11.
54. Nguyen HT, Liu A, Yan D, et al. Sub-bandgap luminescence from doped polycrystalline and amorphous silicon films and its application to understanding passivating-contact solar cells. *ACS Appl Energy Mater*. 2018;1(11):6619-6625.
55. Park H, Bae S, Park SJ, et al. Role of polysilicon in poly-Si/SiOx passivating contacts for high-efficiency silicon solar cells. *RSC Adv*. 2019;9:23261-23266.
56. Schulze TF, Beushausen HN, Leendertz C, Dobrich A, Rech B, Korte L. Interplay of amorphous silicon disorder and hydrogen content with interface defects in amorphous/crystalline silicon heterojunctions Interplay of amorphous silicon disorder and hydrogen content with. *Appl Phys Lett*. 2011;96, 252102(2010):2010-2013.
57. Descoeudres A, Barraud L, De Wolf S, Strahm B, Lachenal D, Ballif C. Improved amorphous/crystalline silicon interface passivation by hydrogen plasma treatment. *Appl Phys Lett*. 2011;99(12):123506.
58. Knights JC, Lucovsky G, Nemanich RJ. Defects in plasma-deposited a-Si: H. *J Non Cryst Solids*. 1979;32(1–3):393-403.
59. Langford AA, Fleet ML, Nelson BP, Lanford WA, Maley N. Infrared absorption strength and hydrogen content of hydrogenated amorphous silicon. *Phys Rev B*. 1992;45(23):13367-13377.
60. Kazahaya T, Hirose M. Coordination Number of doped boron atoms in photochemically-deposited amorphous silicon studied by X-ray photoelectron spectroscopy. *Jpn J Appl Phys*. 1986;25, no. Part 2, No. 1:L75-L77.
61. Lee S, Park S, Park J, et al. The effect of carrier injection stress on boron-doped amorphous silicon suboxide layers investigated by X-ray photoelectron spectroscopy. *Jpn J Appl Phys*. 2011;50, no. 9 PART 1 (9R):95801.
62. Matsuda A. Growth mechanism of microcrystalline silicon obtained from reactive plasmas. *Thin Solid Films*. 1999;337(1–2):1-6.
63. Rezek B, Stuchlík J, Fejfar A, Kočka J. Microcrystalline silicon thin films studied by atomic force microscopy with electrical current detection. *J Appl Phys*. 2002;92(1):587-593.
64. Azulay D, Millo O, Balberg I, Chu V, Conde JP. Current routes in hydrogenated microcrystalline silicon. *Phys Rev B*. 2005;71(11):3-6.
65. Kim S, Park J, Phong PD, Shin C, Iftiquar SM, Yi J. Improving the efficiency of rear emitter silicon solar cell using an optimized n-type silicon oxide front surface field layer. *Sci Rep*. 2018;8(1):1-10.
66. Fell A. A free and fast three-dimensional/two-dimensional solar cell simulator featuring conductive boundary and quasi-neutrality approximations. *IEEE Trans Electron Devices*. 2013;60(2):733-738.
67. McIntosh KR, Baker-Finch SC. OPAL 2: rapid optical simulation of silicon solar cells. *Photovoltaic Specialists Conference (PVSC)*. 2012 38th IEEE: Austin, TX, USA; 2012.

How to cite this article: Park HJ, Lee Y, Park SJ, et al. Tunnel oxide passivating electron contacts for high-efficiency n-type silicon solar cells with amorphous silicon passivating hole contacts. *Prog Photovolt Res Appl*. 2019;27:1104-1114. https://doi.org/10.1002/pip.3190